N/S dual-doped KB-decorated $Na_3V_2(PO_4)_2F_3$ as high-performance cathode for advanced sodium storage properties

Jia-le Xu[1] · An-Ping Tang[1] · Qing Wen[2] · Jun-chao Zheng[2] · Lin-Bo Tang[3] · Ying-De Huang[4] · He-zhang Chen[1]

Abstract

$Na_3V_2(PO_4)_2F_3$ (NVPF) with sodium superionic conductor NASICON) structure's quick diffusion channel, high energy density, and high operating voltage make it among the most promising cathode materials for batteries that use sodium ions. But its inadequate inherent electronic conductivity and structural stability hinder its excellent electrochemical performance. In this investigation, N and S co-doped Ketjen Black (NSKB) decorated NVPF cathode material (NVPF@NSKB) was effectively produced using a straightforward sol–gel technique. When NSKB is added, NVPF takes on a loose, porous shape. Improving the conductivity of the material, significantly increasing the contact area between the electrode and the electrolyte, helps the material to perform better electrochemical performance. Compared with the original NVPF@C, NVPF@NSKB shows better charging performance, reaching a capacity of 115.4 mAh g^{-1} at 0.5 C and 103.3 mAh g^{-1} at 25 C. The battery also demonstrates excellent cycling stability. After 500 cycles at 30 C, the battery's capacity remained at 80.7 mAh g^{-1} with minimal capacity loss. This study demonstrates that N and S co-doped KB is an effective strategy to enhance the performance of sodium-ion battery cathode materials, $Na_3V_2(PO_4)_2F_3$.

Introduction

Regarded as clean and renewable energy sources in the realm of new energy, wind power and solar energy have gained significant attention. However, their irregular and intermittent nature poses challenges in integrating them into the power grid, often leading to their classification as waste streams. To fully utilize the potential of wind and solar energy, it is essential to implement energy storage systems. In recent decades, lithium-ion batteries have emerged as a promising method for energy storage, receiving widespread recognition for their long-cycle capabilities and high energy density [1, 2]. However, the rapid development and price increase of lithium can be attributed to the depletion of lithium resources and the extensive use of electronic devices and energy storage systems [3]. As a result, there is an urgent need for affordable next-generation energy storage solutions. Sodium-ion batteries (SIBs) have emerged as a viable alternative due to the abundance of natural sodium resources and their low cost [4, 5]. Due to the similarities in chemical properties between sodium and lithium, as well as their shared group in the periodic table, SIB research has become increasingly attractive [6, 7]. The advancement of SIBs hinges on the development of advanced cathode materials, making it a crucial area of focus. Many studies are currently being conducted to enhance the cathode materials' ability to store sodium, such as layered oxides [8], Prussian blue analogues [9], polyanionic compounds [10], and organic composite materials [11]. Polyanionic compounds have garnered significant interest owing to their diverse structural

✉ Lin-Bo Tang
 tlb943464594@csu.edu.cn

✉ Ying-De Huang
 yingdecsu@foxmail.com

✉ He-zhang Chen
 278789069@qq.com

1 School of Chemistry and Chemical Engineering, Hunan University of Science and Technology, Xiangtan 411201, Hunan, China

2 School of Metallurgy and Environment, Central South University, Changsha 410083, Hunan, China

3 School of Materials and Environmental Engineering, Changsha University, Changsha 410022, Hunan, China

4 School of Materials Science and Engineering, Zhengzhou University, Zhengzhou 450000, Henan, China

composition and remarkable thermal stability, including vanadium-based phosphates, iron-based phosphates, and phosphates composed of other transition metals (Mn, Co, etc.). Iron-based phosphates and mixed phosphates such as $Na_3Fe_2(PO_4)_3$ [12], $Na_3Fe_2(PO_4)(P_2O_7)$ [13], and especially $Na_4Fe_3(PO_4)_2(P_2O_7)$ [14–16], due to their cost-effectiveness and high structural stability, are now favored by many scholars and have achieved significant results. Because of its great structural integrity, huge gap, and high energy density, $Na_3V_2(PO_4)_2F_3$ (NVPF) in the NASICON structure has also attracted a lot of interest [11]. It features a three-dimensional structure in which $[V_2O_8F_3]$ dioctahedral units are bridged by $[PO_4]$ tetrahedral units, forming large gaps that facilitate sodium ion migration. NVPF features an energy density of 507 Wh kg^{-1} and a typical operating voltage of up to 3.95 V, comparable to the LiFePO$_4$ material (530 Wh kg^{-1}) in commercial lithium-ion batteries [17, 18]. Nevertheless, the $[PO_4]$ tetrahedron's low electrical conductivity (10^{-12} S cm^{-1}) due to its insulating characteristic severely restricts its total electrochemical performance. Thus, in order to enhance electrochemical performance, electrical conductivity must be raised. Strategies to address this issue include conductive carbon coating [19], element doping [20, 21], and designing various morphologies [22, 23]. By employing one or more of the above strategies, effective improvements can be made to the material's electrochemical stability. Because of its enhanced conductivity, affordability, and strong chemical stability, conductive carbon coating has garnered a lot of interest. By preventing the expansion of crystal size, carbon coatings can decrease grain size and increase electrical conductivity [24]. For example, Wang's group prepared a carbon-modified $Na_3V_2(PO_4)_2F_3$ nanocomposite that exhibits a 100th capacity of about 112 mA h g^{-1} at 1 C [25]. Zhang et al. [26] obtained a NVPF nanoparticle composite firmly fixed on carbon nanosheets and reduced graphene oxide through in situ redox reaction, which demonstrated notable rate capability and cyclic stability because of the lowered sodium ion and electron transport distance. KB is an efficient conductive material. KB has a relatively narrow pore size distribution and can act as a conductive bridge to form more conductive paths. In order to enhance composites' electrochemical performance, several researchers have employed KB as a carbon template. Because of their superior electrical conductivity and practical electrode/electrolyte interface, doped carbons including nitrogen, sulfur, and boron have been proposed as an appealing coating framework to enhance the performance of battery electrode materials. Simultaneously, doping has the potential to augment the carbon layer's active sites, thus amplifying the material's electrical conductivity and sodium storage capability. Li et al. [27] synthesized fibrous NVPF by electrospinning technique using polyvinylpyrrolidone as the nitrogen source. Defects in the carbon layer increased as a result of nitrogen

atom doping. The enhanced material shows excellent electrochemical performance and cycle stability.

Thus, the sulfur and nitrogen were obtained from thiourea, while the carbon came from KB. A nitrogen-sulfur co-doped KB-coated NVPF cathode material (NVPF@NSKB) was prepared through sintering. More cracks and hotspots in the carbon layer are created by the start of thiourea, which speeds up the flow of electrons and Na ions and enhances the cycle performance and rate capability of the NVPF. As expected, the nitrogen-sulfur co-doping modified KB strategy enable the NVPF@NSKB electrode demonstrates remarkable potential with a superb electrochemical output.

Experimental section

Materials preparation

Nitrogen-sulfur co-doped KB-coated $Na_3V_2(PO_4)_2F_3$ composite material was prepared via a basic sol–gel technique. Citric acid monohydrate used as a chelating agent, reducing agent, and thiourea is utilized as a source of sulfur and nitrogen and as a carbon source. Typically, 60 ml of ultrapure water were used to dissolve 0.612 g of citric acid monohydrate. Next, 0.468 g of NH_4VO_3 were added, and the liquid was stirred at 80 °C until it turned a deep blue color. The mixture was then stirred for 30 min while 0.46 g of $NH_4H_2PO_4$ and 0.252 g of NaF were added in turn. Subsequently, the ultrasonic-treated KB and thiourea blend was included into the amalgamation. To obtain the precursor, the mixture was continuously stirred at 80 °C until a blue gel formed. It was then placed in a vacuum drying oven at 120 °C for 12 h. After that, the ground precursor was transferred to a tubular furnace where it underwent a 4-h pretreatment at 300 °C under Ar gas protection and, after that, for eight hours, further annealed at 600 °C while shielded by Ar gas. When the material spontaneously cooled to room temperature, the nitrogen-sulfur co-doped KB-coated $Na_3V_2(PO_4)_2F_3$ composite material (NVPF@NSKB) was created.

Pure carbon-coated sample NVPF@C, KB-coated sample NVPF@KB, and nitrogen-doped KB-coated sample NVPF@NKB were prepared using the same method. NVPF@C omitted the addition of KB and thiourea, NVPF@KB did not include thiourea, while NVPF@NKB replaced thiourea with urea.

Structural and electrochemical characterization

Using powder-XRD measurements, the purity of the generated materials was assessed using the Rigaku MiniFlex 600 X-ray diffractometer. A 2θ-angular range of 10–90° was covered at a pace of 5°min^{-1} while the data was being taken

at room temperature. Fourier-transform infrared absorption spectra were measured with the Nicolet Nexus 470 equipment to investigate the chemical bonding of the materials in the 500–2000 cm^{-1} area. The Jobin–Yvon LabRAM HR-800 spectrometer was used to examine the properties of carbon hybridization in each sample. The ASAP 24603.01 device was used to conduct N$_2$ adsorption–desorption studies in order to measure the samples' specific surface area and examine their pore sizes. The elemental valence states of every sample were examined using the ESCALAB 250XI XPS Thermo instrument. The Hitachi Regulus 8100 scanning electron microscope and the JEOL 2100F transmission electron microscope were used to perform microscopic examinations of all the materials.

Electrochemical measurements

The CR2025 coin cells, whose approximate mass of active material ranged from 1.1 to 1.5 mg, were used for all electrochemical characterizations. The specific area of stage is 1.1304 cm^2. With an equal mass ratio of 7:1.5:1.5, the conductive agent, acetylene black, and the active substance, binder (PVDF), were mixed together. The NVPF cathode electrode was created by coating aluminum foil current collectors with a uniformly mixed slurry that had been solventized and agitated the mixture at 80 °C until it became deeply blue.ne. This was followed by eight hours at 120 °C of vacuum drying of the slurry. A mixture of solvents (EC:DEC = 1:1 vol%) dissolved NaClO$_4$ was used as the electrolyte, glass fiber was employed as the separator, and metallic sodium foil had the role of the anode. A glovebox with a Mikrouna Super pure argon was used to construct the cells. In the voltage range of 2.0–4.3 V, tests of constant current charge/discharge at various rates and the galvanostatic

intermittent titration method (GITT) were carried out using a BlueDrive battery testing apparatus CT2001A (Wuhan, China). Utilizing an electrochemical workstation (CHI 760E), multiple scans Measurements were carried out using cyclic voltammetry at scan speeds between 0.1 and 5.0 mV s^{-1}. The same equipment was used for electrochemical impedance spectroscopy (EIS) tests, having an amplitude of 5 mV and frequencies ranging from 0.01 Hz to 100 kHz.

Results and discussion

The schematic illustration of the procedure for preparation is exhibited in Fig. 1. KB was combined with citric acid, ammonium metavanadate, thiourea, and ammonium dihydrogen phosphate to synthesize NVPF@NSKB by a simple sol–gel technique. As a reducing agent, citric acid is employed, and carbon comes primarily from KB. Thiourea provides both components needed for co-doping of nitrogen and sulfur.

The XRD patterns of NVPF@C, NVPF@KB, NVPF@ NKB, and NVPF@NSKB composites are shown in Fig. 2a. The peaks of diffraction of all samples are similar to Na$_3$V$_2$(PO$_4$)$_2$F$_3$ standard card (JCPDS No.89–8485) with NASICON structure, and the background peaks near 2θ = 35.6° are related to Na$_3$V$_2$(PO$_4$)$_3$, indicating that the introduction of KB, N, and S have no effect on the NVPF's lattice structure. Furthermore, in the samples, no carbon-derived peaks are found, indicating that carbon derived from citric acid, urea, and thiourea decomposition and added KB exist in an amorphous form. Figure 2b and c show the refined XRD patterns of NVPF@C and NVPF@NSKB. The results reveal that their structure both belong to the tetragonal crystal system with space group *P*42/*mnm*. The lattice
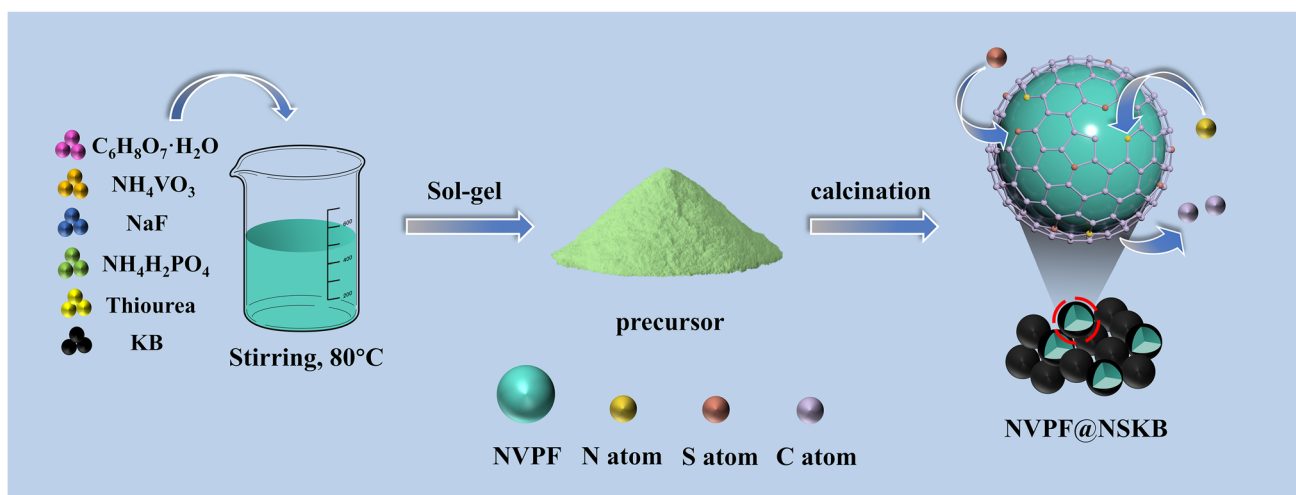

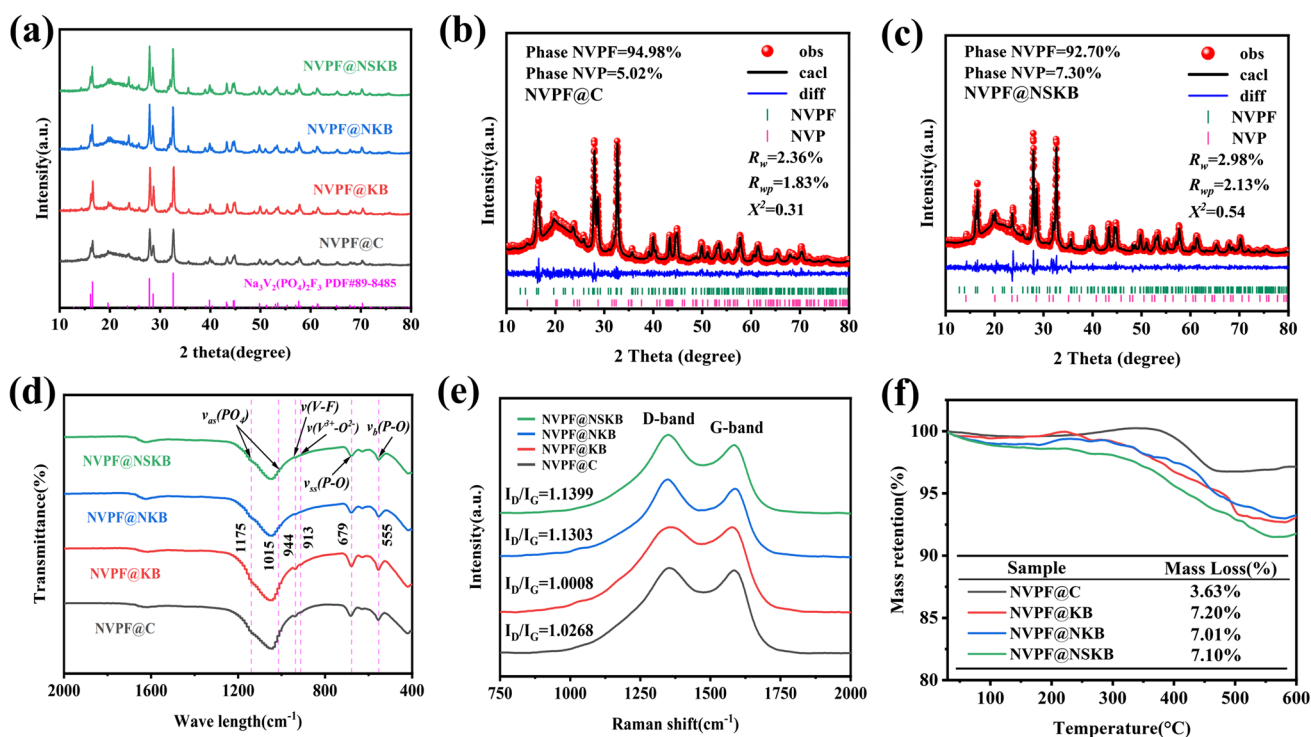**Fig. 1** Shows the schematic diagram of its preparation

Fig. 2 **a** XRD patterns, Rietveld refinement of the X-ray diffraction pattern of **b** NVPF@C and **c** NVPF@NSKB. **d** FT-IR spectra, **e** Raman spectra, and **f** TGA curves of NVPF samples

parameters of NVPF@C are $a = 9.034$ Å, $b = 9.034$ Å, and $c = 10.728$ Å, which are extremely close to NVPF@NSKB ($a = 9.036$ Å, $b = 9.036$ Å, $c = 10.742$ Å). The percentage of heterophase $Na_3V_2(PO_4)_3$ in the two materials is 5.02% and 7.30%, respectively. The FT-IR spectra characterizing the molecular structures of each material are shown in Fig. 2d. A vibration of V^{3+}-O^{2-} bonds in VO_6 octahedra is assigned to the band at 913 cm^{-1}, whereas the V-F bond is associated with the band at 944 cm^{-1}. The bands between 1015 and 1175 cm^{-1} and at 679 and 575 cm^{-1} relate to PO_4 tetrahedra [28]. NASICON structure NVPF has been effectively synthesized, according to the combination of the XRD and FT-IR spectra data.

Using Raman spectroscopy, the hybridization characteristics of the carbon in each sample were examined (Fig. 2e). Two noticeable vibrational peaks can be found at 1348 cm^{-1} and 1582 cm^{-1}, which are indicative of disordered graphite carbon (D band, sp^3 carbon atoms) as well as the carbon that has a high level of crystalline graphitization (sp^2 carbon atoms, G band) [29]. The amount of graphitization of carbon in the samples is indicated by the I_D/I_G ratio. The findings show that the NVPF@KB composite material has a lower I_D/I_G intensity ratio (1.0008) than the NVPF@C composite material (1.0268), indicating that the addition of KB is responsible for the decreased amount of disordered carbon in the NVPF@KB composite material and its improved

electronic conductivity against NVPF@C. However, the I_D/I_G intensity ratio of NVPF@NKB (1.1303) and NVPF@NSKB (1.1399) is higher than that of NVPF@KB (1.0008), attributed to the nitrogen and sulfur doping. It may produce additional carbon layer active sites and non-intrinsic flaws, promoting sodium ion migration [30, 31]. Additionally, the I_D/I_G intensity ratio of NVPF@NSKB is larger than that of NVPF@NKB because of the synergistic impact of N and S dual-atom doping, which can induce more defects than nitrogen doping alone. Thermogravimetric analysis was used to examine each composite material's carbon content. Figure 2f illustrates how carbon combustion and adsorbed water evaporation are linked to weight loss below 350 °C and between 350 and 550 °C, respectively. According to calculations, the precise carbon contents of NVPF@C, NVPF@KB, NVPF@NKB, and NVPF@NSKB are 3.63%, 7.20%, 7.01%, and 7.10%, respectively.

When the temperature rises, thiourea releases carbon nitride compounds like C_2N^{2+}, C_3N^{2+}, and C_3N^{3+} in addition to gases like NH_3 and H_2S. It interacts with porous KB during heat treatment to produce sources of sulfur and nitrogen, which results in the production of goods that are doped with sulfur and nitrogen content. material KB, nitrogen-sulfur-doped KB is compounded with NVPF to form the NVPF@NSKB sample. XPS was used to validate the existence of Na, S, C, and N elements in order to further examine the surface

electronic states and the chemical status of the elements in the NVPF@NSKB sample (Fig. 3). The complete spectrum (Fig. 3a) shows the presence of the distinctive peaks for Na 1 s, V 2p, P 2p, O 1 s, F 1 s, N 1 s, C 1 s, and S 2p, further demonstrating the effective fabrication of NVPF@NSKB. Following fitting, Fig. 3b displays the C 1 s XPS spectrum of NVPF@NSKB. The peaks at 284.8, 285.4, and 288.7 eV, respectively, correspond to C–C, C-O/C-N/C-S, and C=O bonds. Pyridinic, pyrrolic, and graphitic nitrogen are represented by three peaks in the N 1 s spectra (Fig. 3c) at 398.4, 400.6, and 405.6 eV, respectively. These peaks show that nitrogen was successfully doped into the carbon layer. The addition of sulfur to the carbon layer is confirmed by peaks in the S 2p spectra (Fig. 3d) at 163.9 and 167.8 eV, which correspond to S–O and S–C–S bonds. The insertion of C, N, and S does not change the valence state of V^{3+} in NVPF, as evidenced by the V 2p spectra (Fig. 3e), which displays typical peaks of V^{3+} at V $2p_{1/2}$(517.1 eV) and V $2p_{3/2}$(524.6 eV) [30].

Using the nitrogen adsorption–desorption isotherms approach, every sample's specific surface area and pore size distribution were looked at, as illustrated in Fig. 4a–d. Each and every sample showed type IV isotherms, indicating mesoporous characteristics. The results show that the specific surface areas and average pore sizes of NVPF@C, NVPF@KB, NVPF@NKB, and NVPF@NSKB are 21.3945, 44.5890, 66.2861, and 94.2253 m^2 g^{-1}, and 15.0501, 8.4530, 7.3725, and 5.1424 nm, respectively. Among them, NVPF@NSKB has the largest specific surface area, which is 4.4 times that of NVPF@C. From the above results, it can be observed that the pore size of NVPF@C, NVPF@KB, NVPF@NKB, and NVPF@ NSKB continuously decreases, and within the entire pore size range of 5 to 20 nm, NVPF@NSKB with the smallest pore size exhibits the largest pore volume among all materials, indicating a significant improvement in the material's porosity. First of all, owing to its remarkable properties, including an extensive specific surface area, a porous structural configuration, and exceptional conductivity, KB (Ketjen Black) stands out as an ideal carbon source for various applications. Second, gases like NH_3 and H_2S as well as nitrogen-carbon compounds like C_2N^{2+}, C_3N^{2+}, and C_3N^{3+} are released during the breakdown of thiourea. During the heat treatment process, they react with porous KB to create an even more porous structure. Enhancing the specific surface area is a desirable approach as it increases the contact interface between the electrolyte and electrode material, thereby facilitating improved interaction and performance. This augmentation of the specific surface area promotes better conductivity and efficiency in the overall system.
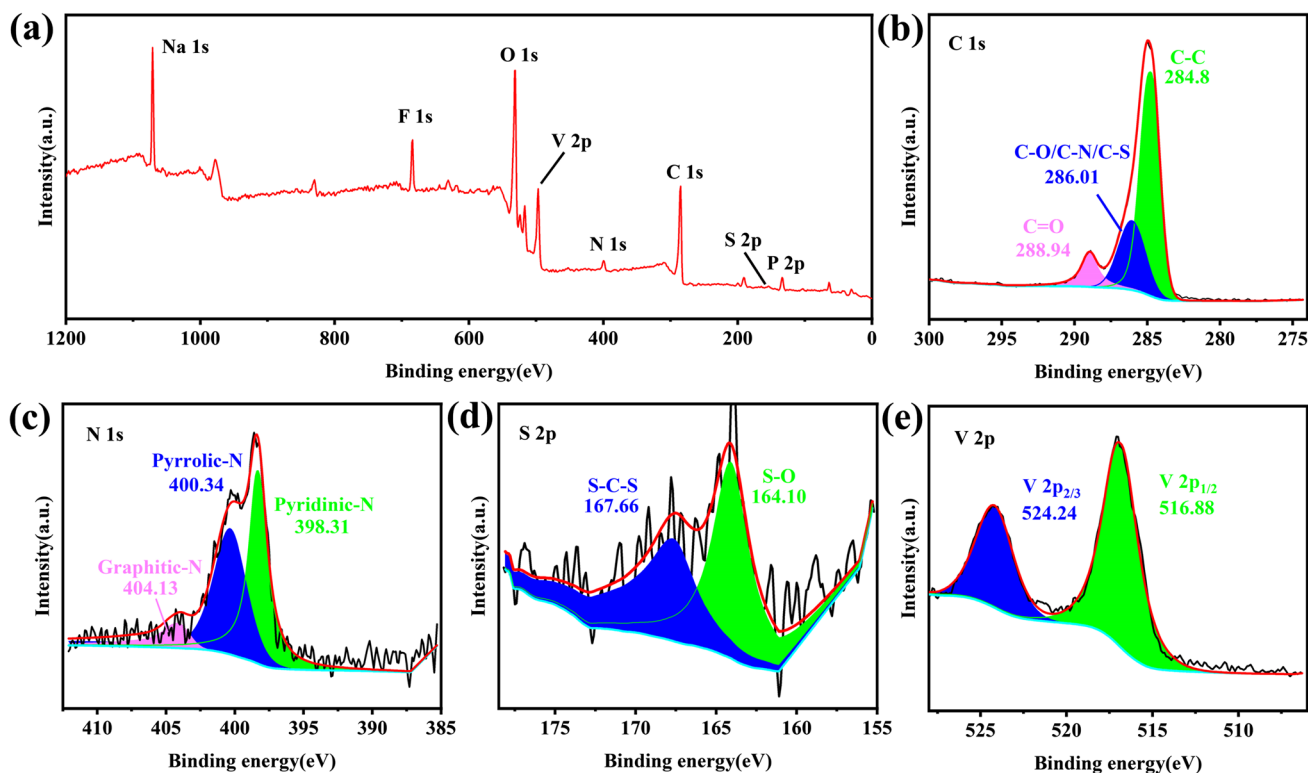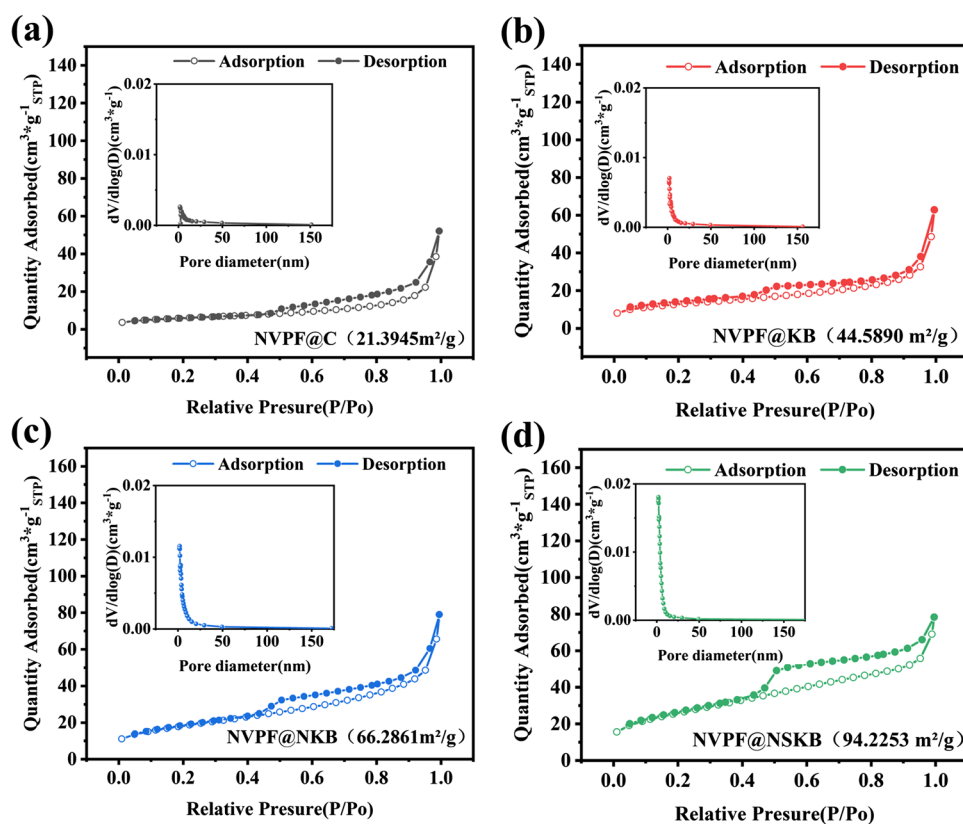

Fig. 3 **a** Full-XPS spectra of NVPF@NSKB. High-resolution **b** C 1 s, **c** N 1 s, **d** S 2p, **e** V 2p spectra of the NVPF@NSKB

Fig. 4 The nitrogen adsorption–desorption curves of **a** NVPF@C, **b** NVPF@KB, **c** NVPF@NKB, and **d** NVPF@NSKB, and pore-size Distribution plots are inserted in

In order to study the impact of the introduction of different elements doped KB on the morphology of the material. The as-prepared NVPF@C, NVPF@KB, NVPF@NKB, and NVPF@NSKB composites were further examined by SEM, as showed in Fig. 5. Compared to NVPF@C (Fig. 5a), NVPF@KB (Fig. 5b), NVPF@NKB (Fig. 5c), and NVPF@NSKB (Fig. 5d) evidently exhibit more pores overall. This is attributed to the uniform dispersion of microsphere-shaped KB, which serves as a suitable substrate for the growth of NVPF particles, thereby reducing particle aggregation and enriching the inter-particle pores. Compared to NVPF@KB, NVPF@NKB and NVPF@NSKB have less particle aggregation, and higher porosity, consistent with the results of BET testing. This is explained by the heteroatom-doped carbon layer's ability to limit the formation of NVPF crystal particles and supply more defects and nucleation sites, thereby effectively mitigating the agglomeration phenomenon during the thermal process. The porous structure of NVPF@NKB and NVPF@NSKB composites can shorten the migration distance of sodium ions in the embedding/removal process, and widen the area where the electrolyte and electrode material come into contact. Enhancing the surface area can lead to improved electrochemical performance of materials by facilitating effective ion diffusion and promoting better interaction between the electrode and electrolyte. Figure 5e presents the mapping result for NVPF@NSKB, where it is evident that the eight elements—C, N,

S, Na, V, P, O, and F—are uniformly distributed throughout the NVPF@NSKB composition. The results of the SEM mapping and XPS mapping clearly support the presence of C, N, and S in NVPF@NSKB.

Figure 6 displays the usual TEM pictures of the composite at various magnifications. As shown in Fig. 6a–c, NVPF@NSKB particles are enveloped by a carbon layer approximately 3 nm thick, which facilitates electron transfer and provides buffering for the volume changes of active materials caused by sodium ion deintercalation, thereby enhancing structural stability. And a uniform carbon coating layer can decrease the cathode material's deterioration by the electrolyte and improve the battery's cycle performance. Lattice fringes with a d-spacing of 0.328 nm are clearly seen in Fig. 6c, corresponding to the (103) plane of the typical NASICON structure of NVPF.

Further research was done on the electrochemical characteristics of the composite electrodes made of NVPF@NSKB. Using cycle performance, rate performance, and cyclic voltammetry tests, the electrochemical characteristics of the four NVPF composite materials were examined. The first three cycles of each NVPF composite's cyclic voltammetry (CV) curves at 0.2 mV s^{-1} are displayed in Fig. 7a–d. The redox reactions of V^{3+} and V^{4+} are shown by two pairs of redox peaks in the image, which are situated at approximately 3.7 V and 4.2 V. During the reaction, Na$^+$ enters and exits the NVPF structure at two
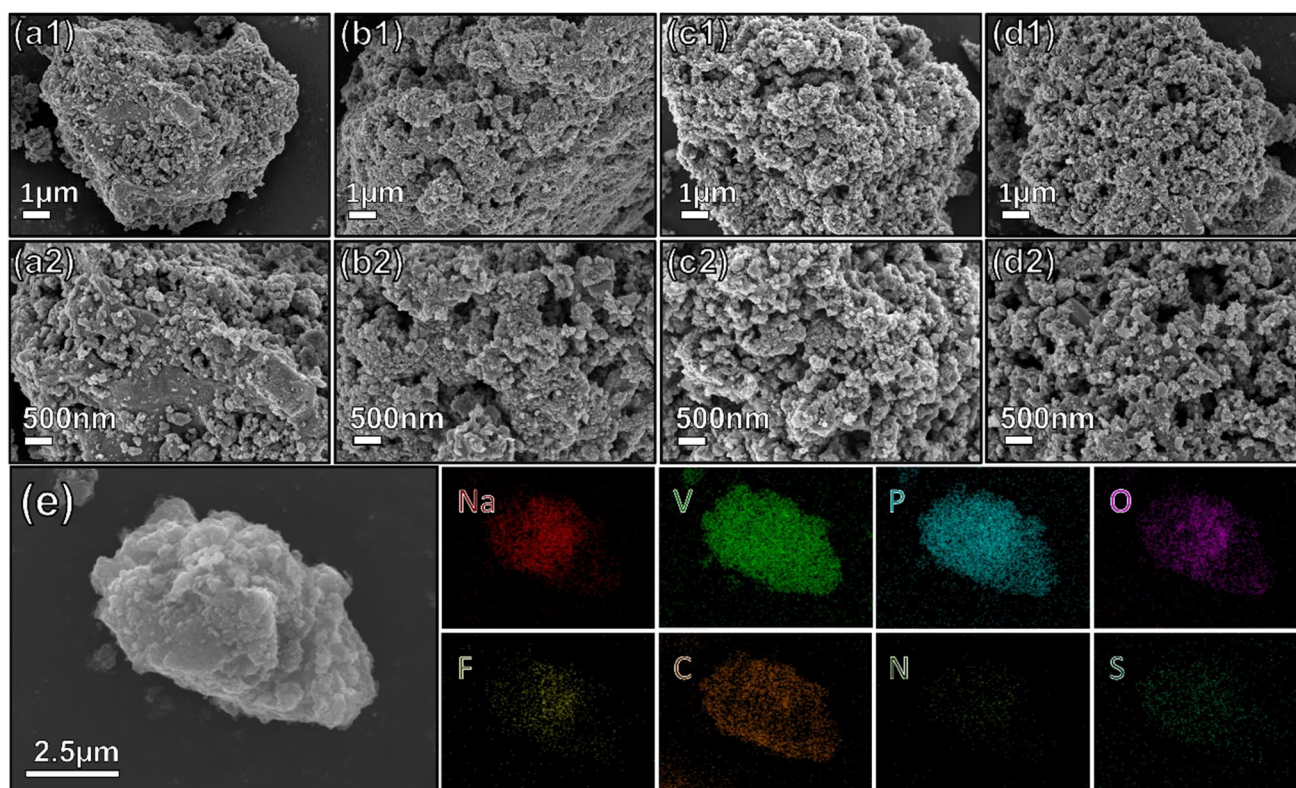
Fig. 5 SEM images of NVPF@C (**a1–a2**), NVPF@KB (**b1–b2**), NVPF@NKB (**c1–c2**), and NVPF@NSKB (**d1–d2**). **e** The elemental mapping of NVPF@NSKB

distinct locations. The redox peak located around 3.4 V is attributed to the NVP impurity phase generated by the fluorine lost during calcination at high temperatures [32]. Each NVPF composite material's initial three-cycle CV curves essentially overlap, demonstrating the materials' strong reversibility.

The parameters of magnification for several NVPF composites are displayed in Fig. 7e. According to the figure, the specific discharge capacities of NVPF@C, NVPF@KB, and NVPF@NKB are 101.9, 108.9, and 103.7 mA h g^{-1}, respectively, at a current density of 0.5C. 115.4 mA h g^{-1} is the greatest specific discharge capacity for NVPF@NSKB. From 0.5 to 25 C (1C = 110 mA g^{-1}), the discharge capacity released by NVPF@C decreases significantly. Only 39.9 mA h g^{-1} is the specific capacity at 25.0 C, substantially less than NVPF@KB (74.9 mA h g^{-1} at the same rate), NVPF@NKB (93.4 mA h g^{-1}), and NVPF@NSKB (103.3 mA h g^{-1}). Among them, NVPF@NSKB has the best magnification performance, high specific discharge capacities of 115.4, 114.2, 112.6, 108.9, 106.1, 104.9, 105.2, and 103.3 mA h g^{-1} are released at current densities of 0.5, 1.0, 2.0, 5.0, 10.0, 15.0, 20.0, 25.0C. Significantly greater than other materials at the same magnification. The NVPF@NSKB electrode has the ability to recover 107.9 mAh g^{-1} (0.5 C) in particular after cycling at various current densities. The

best electrochemical performance of all the electrodes was discovered to be displayed by the NVPF@NSKB electrode.

Figure 8b–c and e–f illustrate the charge/discharge curves for NVPF@C, NVPF@KB, NVPF@NKB, and NVPF@NSKB at current densities of 1 C and 10 C, respectively, for the first cycle and the 100th cycle. The charge–discharge curves obtained at 1 C exhibit distinct plateaus in the vicinity of 3.4 V, 3.6 V, and 4.1 V. Notably, the first two plateaus align with the two phases associated with Na$^+$ insertion/extraction from the Na2 sites. Furthermore, the plateau observed around 4.1 V corresponds to the redox peak observed in the CV curves and represents the second Na + insertion into or extraction from the Na1 sites (Fig. 7a–d). Because polarization occurs at high current densities, the plateau is less visible with a current density of 10 C. It can be clearly observed in Fig. 8f that after 100 cycles, the charge–discharge curve of NVPF@C is severely deformed, indicating its weak anti-polarization ability. The cycle performance of the four NVPF composite materials was evaluated at varying current densities. The results revealed that NVPF@NSKB exhibited stable long-term cycle performance across different current densities. As depicted in Fig. 8a, the initial specific capacity of NVPF@C at 1 C was 91.4 mAh g^{-1}. After 100 cycles, the specific capacity remained at 72.3 mAh g^{-1}, corresponding to a capacity retention rate of 79.1%.

After 100 cycles, NVPF@KB, NVPF@NKB, and NVPF@NSKB had specific capacities and capacity retention rates of 93.5, 99.9, and 111.0 mA h g^{-1} and 92.1%, 92.8%, and 96.8%, respectively. Greater than NVPF@C, among the four NVPF composites, NVPF@NSKB exhibited the best cycle stability, delivering the highest specific capacity of 111.0 mAh g^{-1} and an impressive capacity retention rate of 96.8%. In comparison, NVPF@C, NVPF@KB, and NVPF@NKB exhibited lower specific capacities of 65.8 mAh g^{-1}, 84.8 mAh g^{-1}, and 94.8 mAh g^{-1}, respectively. Remarkably, even at the elevated current density of 10 C, NVPF@NSKB maintained a superior capacity of 101.2 mAh g^{-1} and an excellent capacity retention rate of 99.8% after 100 cycles, further highlighting its exceptional cycle stability. Further, long-term stability data of NVPF@NKB is taken due to its encouraging results. 30 C is a high rate of NVPF@NSKB exhibits amazing long-cycling performance (Fig. 8g). The initial capacity of NVPF@NSKB is 82.6 mA h g^{-1}, and 500 cycles later, it releases a defined 80.7 mAh g^{-1} capacity, with a 97.7% maximum capacity retention rate, with almost no significant fading in capacity.

As mentioned above, the excellent electrochemical performance of NVPF@NSKB benefits from the porous structure of N and S double-doped KB-coated Na$_3$V$_2$(PO$_4$)$_2$F$_3$ particles. The coating of KB on the surface of the material not only alleviates the damage to the material structure and enhances the material's electrical conductivity during the Na$^+$ insertion/extraction process, but also changes the morphology of the material and shortens the transport path of Na$^+$ ions. However, the method of N and S double doping can introduce a large number of external flaws in KB, effectively improve the reception ability of Na$^+$ ions, and thus significantly improve the magnification and cycling properties of NVPF@NSKB composites.

In order to deeply study the ion diffusion/migration dynamics of Na$^+$ in each composite material, cyclic voltammetry tests were performed on the four prepared NVPF composites at different scan speeds (Fig. 9a–d). It is evident that as the scan rate increases, so does each material's redox peak current, and as polarization occurs, the anode peak and cathode peak of each material shift toward high voltage and low voltage respectively. Figure 9e–h demonstrate the linear link between the scan speed's arithmetic square root and peak current (V$_{1/2}$), and the diffusion coefficient of sodium ions of each composite material at different redox peak positions is calculated according to the Randles-Sevik formula (Eq. (1)). Table 1 presents the computed results, revealing that the diffusion coefficient of NVPF@C exhibits the smallest value at the O1 peak position. Interestingly, the diffusion coefficients of the other composite materials are found to be essentially identical at this particular point. At the O2 and R1 peaks, the diffusion coefficients of each material increase sequentially, and the diffusion coefficient of NVPF@NKB is the largest at the

Table 1 D$_{Na+}$ calculation results and EIS fitting results of REDOX peaks of each material

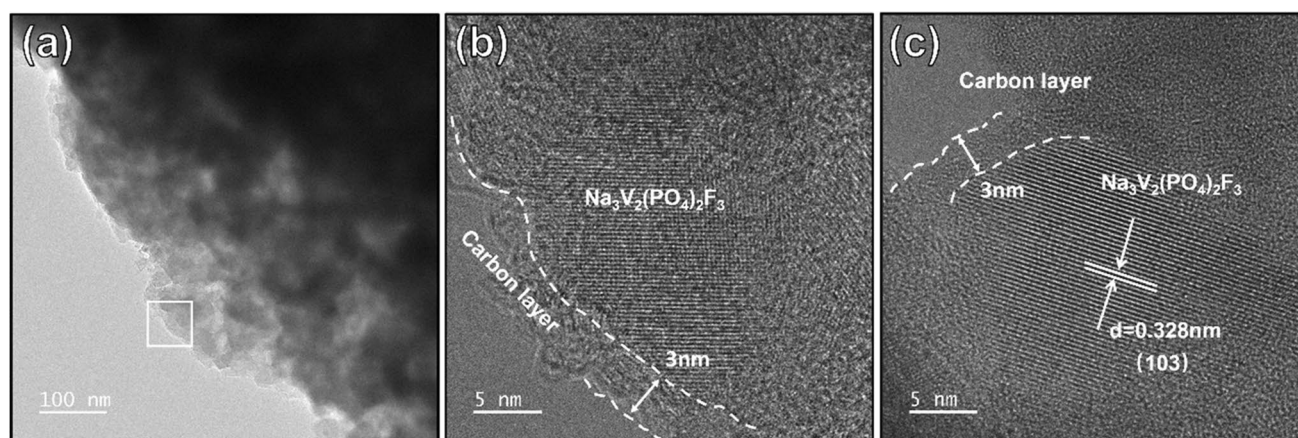| Sample	D$_{Na+}$ at O1 (cm^2/s)	D$_{Na+}$ at O2 (cm^2/s)	D$_{Na+}$ at R1 (cm^2/s)	D$_{Na+}$ at R2 (cm^2/s)	Rs(Ω)	Rct(Ω)
NVPF@C	1.52E-11	1.30E-11	3.82E-12	3.49E-13	12.30	475
NVPF@KB	1.95E-11	1.35E-11	7.04E-12	3.36E-12	9.90	286
NVPF@NKB	1.86E-11	1.38E-11	8.93E-12	5.53E-12	16.30	272.60
NVPF@NSKB	1.98E-11	1.44E-11	1.01E-11	4.92E-12	17.79	68.08

Fig. 6 TEM images of NVPF@NSKB

Fig. 7 CV curves of **a** NVPF@C, **b** NVPF@KB, **c** NVPF@NKB, and **d** NVPF@ NSKB when scanning at the speed of 0.2 mV s^{-1}. **e** Four samples' performances are rated at varying rates. **f** NVPF@ NSKB charge–discharge curves at various rates
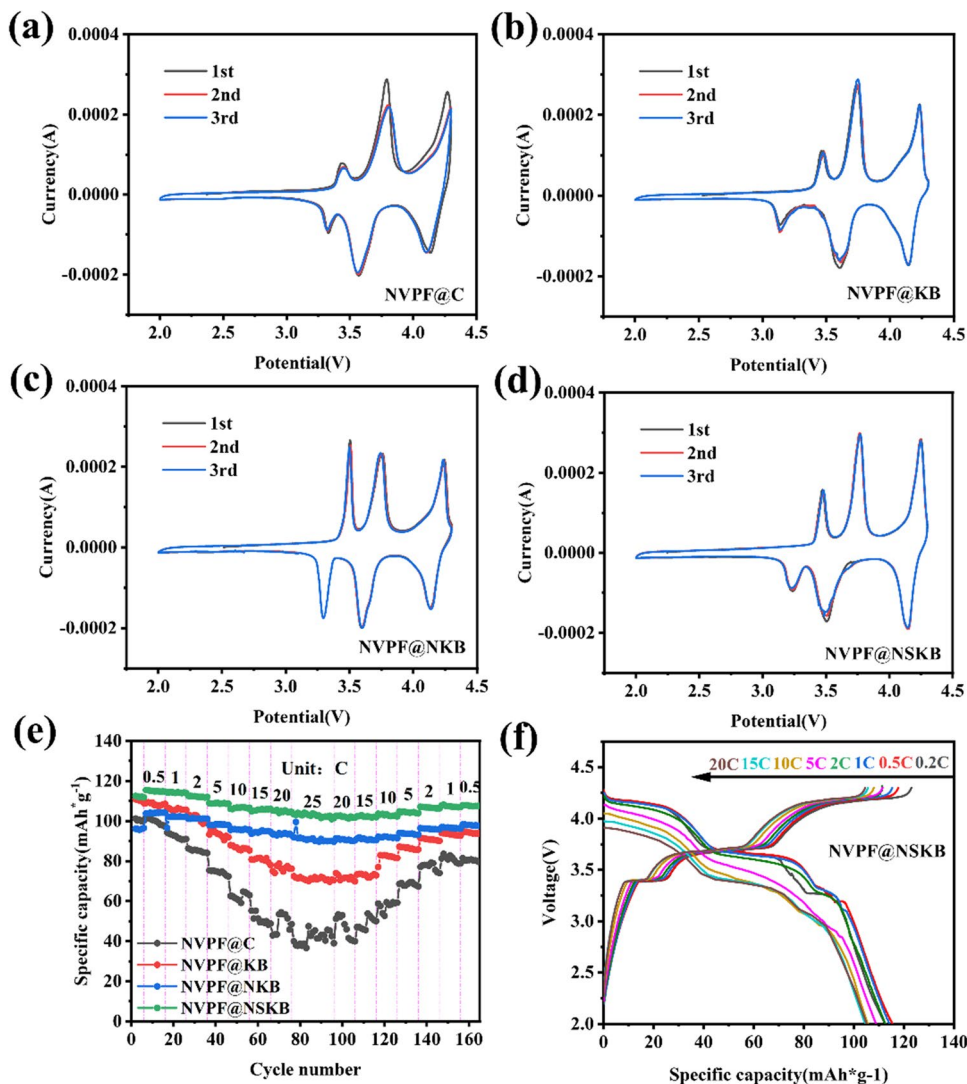
R2 peak. However, based on the comprehensive results, the diffusion coefficient of NVPF@NSKB increases in each redox peak and has the best ion diffusion performance, followed by NVPF@NKB and NVPF@C has the worst ion diffusion performance.

$$I_p = 2.69 \times 10^5 n^{3/2} A C D_{Na^+}^{1/2} v^{1/2} \qquad (1)$$

$$D_{Na^+} = \frac{4}{\pi \tau} \left(\frac{m V_m}{MS} \right)^2 \left(\frac{\Delta E_S}{\Delta E_\tau} \right) \qquad (2)$$

To comprehend the impact of N and S double-doped KB on the kinetics of reactions and charge transfer in NVPF composites, electrochemical impedance test (EIS), and constant current batch titration test (GITT) were performed. Figure 10a presents the AC impedance curves for each sample. In the high and low-frequency regions, the semicircles and straight lines correspond to the charge

transfer resistance (Rct) and the diffusion impedance associated with sodium ion diffusion, respectively. The element Zw is related to diffusion resistance, CPE represents the double-layer capacitance, and Rs denotes the combined resistance of the separator and electrolyte solution. Table 1 summarizes the resulting solution resistance (Rs) and charge transfer resistance (Rct) values. The fitting of these impedance data was performed using the equivalent circuit model depicted in Fig. 10b. The electrode interface's charge transfer velocity of NVPF@NSKB has increased significantly, as indicated by the lowest Rct value of 68.08Ω.

During 25 min, the battery in the GITT experiment was charged and drained at a constant current of 0.1 C, and the step was repeated after standing for 120 min. The D$_{Na+}$ of each NVPF composite was calculated by Eq. (2), and the calculation results were shown in Fig. 11. As can be seen from Fig. 10, D$_{Na+}$ of NVPF@NSKB and NVPF@ NKB is more concentrated than that of NVPF@KB and
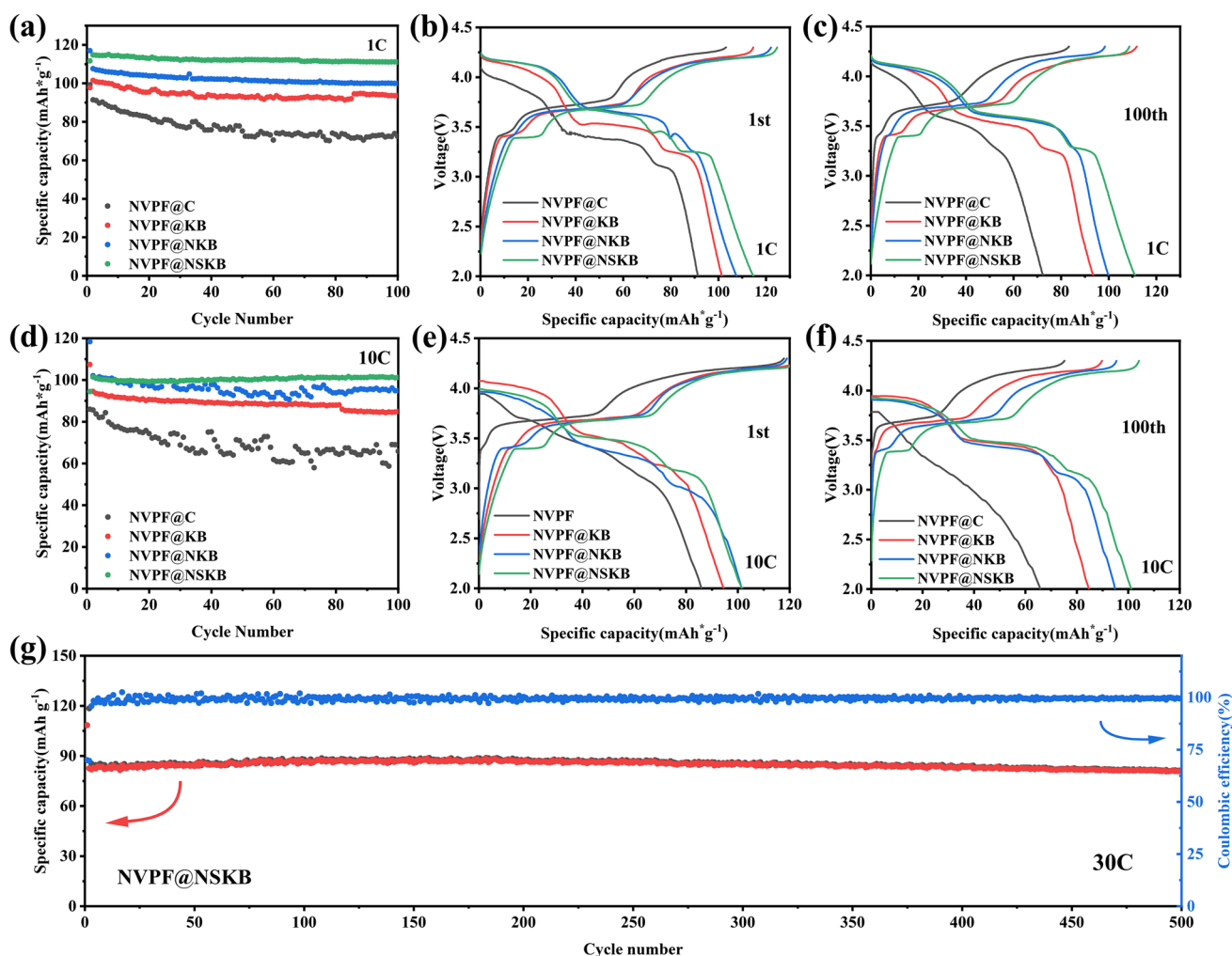
Fig. 8 Cyclic performances (**a**), initial charge–discharge curves (**b**), and 100th charge–discharge curves (**c**) at 1C for the NVPF samples. NVPF samples at 10C: cyclic performances (**d**), initial charge and discharge curves (**e**), and 100th charge–discharge curves (**f**). **g** NVPF sample performance throughout a prolonged cycle at 30C

NVPF@C, primarily within the region of 10^{-11}–10^{-12} cm^2 s^{-1}. indicating that NVPF@NKB and NVPF@NSKB have faster ion migration degrees. Due to the different calculation methods, the diffusion coefficient calculated by GITT is not the same as that of CV. However, this does not stop the relative relationships between the diffusion coefficients of different materials from being compared. The influence of N and S double-doped KB on the material's structure accounts for NVPF@NSKB's superior ion diffusion capacity (D_{Na+}) and lowest electrochemical impedance (EIS), as indicated by the following data. The material's ion diffusion and reaction kinetics are impacted by the porous structure made of N and S double-doped KB, which shortens the Na$^+$ transport channel, expands the material's surface area in contact with the electrolyte, and provides more reactive sites. These benefits significantly encourage the material's electrochemical characteristics to develop.

Conclusion

To summarize, the N, S co-doped KB-coated NVPF cathode was effectively produced with a straightforward sol–gel technique. The findings show that adding KB improves the material's electrical conductivity and successfully prevents particle agglomeration, resulting in a porous structure. Simultaneously, N and S co-doping generate more defects and active sites on KB. These defects serve as substrates for material growth, inhibit aggregation of particle, further increase the material's porosity, and significantly shorten the Na ion diffusion migration
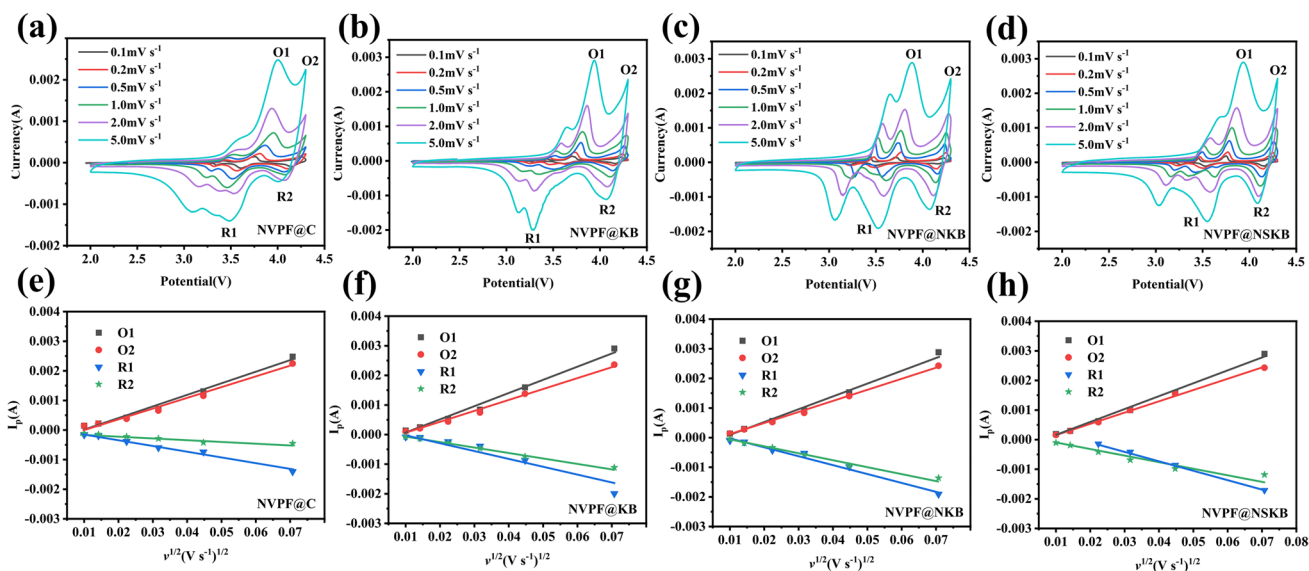
Fig. 9 **a–d** show the square root of the scan rate at different peak sites and peak currents in a linear relationship, and **e–h** show the CV curves of NVPF samples between 0.1 and 5 mV s^{-1} at different scan rates

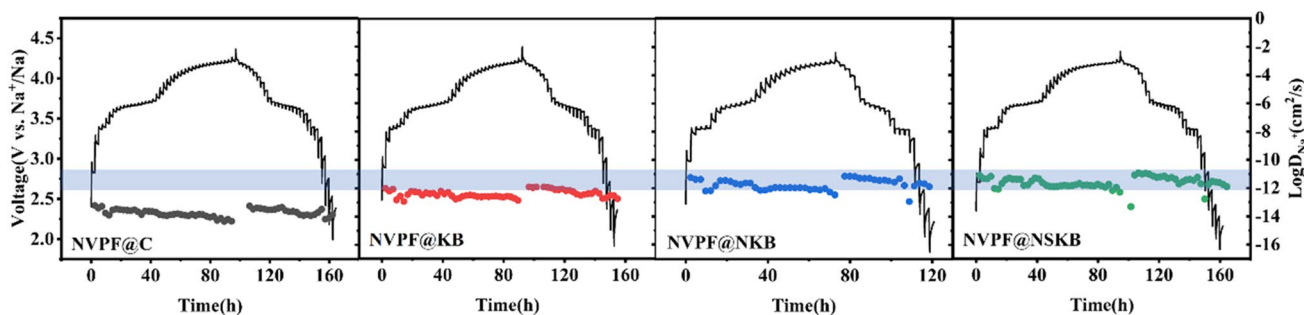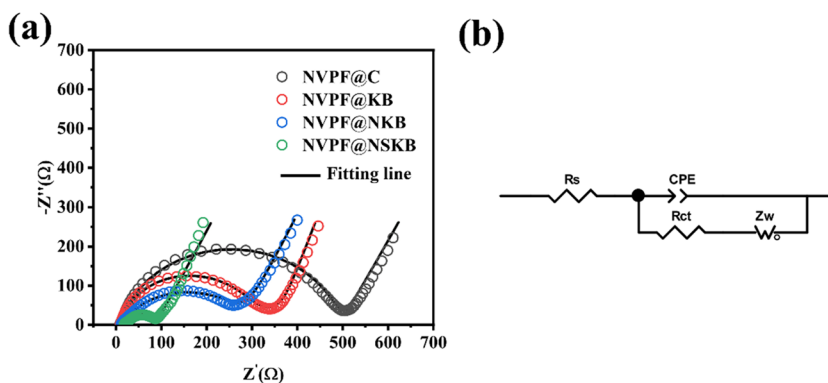**Fig. 10** **a** Nyquist plots of NVPF samples along with matching fitting curves. **b** The corresponding circuit model that fits the EIS

Fig. 11 GITT profiles of NVPF samples and the associated sodium ion diffusion coefficients

path. The increase in active sites facilitated by the N, S co-doped KB coating on the NVPF cathode accelerates the charge transfer between the cathode and electrolyte. Consequently, the N, S co-doped KB-coated NVPF cathode exhibits improved charge transfer kinetics and Na ion

diffusion kinetics, leading to excellent electrochemical performance. Notably, this material delivers a high initial reversible specific capacity of 115.4 mAh g^{-1} at a 0.5 C rate and maintains a remarkable specific capacity of 103.3 mAh g^{-1} even at the elevated 25 C rate. Furthermore, it

demonstrates exceptional cycle life, retaining a specific capacity of 80.7 mAh g^{-1} after 500 cycles at an enhanced 30 C rate, with an impressive capacity retention rate of 97.7%. Consequently, the technique of double-doping KB with N and S as a coated carbon layer offers a useful way to enhance the NVPF cathode's electrochemical performance.

Declarations

Competing interests The authors declare no competing interests.

References

1. Liu L, Song T, Han H et al (2015) Electrospun Sn-doped LiTi 2 (PO 4) 3/C nanofibers for ultra-fast charging and discharging. J Mater Chem A 3:10395–10402

2. Wu Y, Liu X, Yang Z et al (2016) Nitrogen-doped ordered mesoporous anatase TiO2 nanofibers as anode materials for high performance sodium-ion batteries. Small 12:3522–3529

3. Kotaka H, Momida H, Oguchi T (2022) Performance and reaction mechanisms of tin compounds as high-capacity negative electrodes of lithium and sodium ion batteries. Mater Adv 3:2793–2799

4. Hwang J-Y, Myung S-T, Sun Y-K (2017) Sodium-ion batteries: present and future. Chem Soc Rev 46:3529–3614

5. Rojo T, Hu YS, Forsyth M et al (2018) Sodium-ion Batteries 8:1800880

6. Wang Q, Ling C, Li J et al (2021) Experimental and theoretical investigation of Na4MnAl (PO4) 3 cathode material for sodium-ion batteries. Chem Eng J 425:130680

7. Wang M, Wang Q, Ding X et al (2022) The prospect and challenges of sodium-ion batteries for low-temperature conditions. Interdisciplinary Mater 1:373–395

8. Wang Y, Xiao R, Hu Y-S et al (2015) P2-Na0. 6 [Cr0. 6Ti0. 4] O2 cation-disordered electrode for high-rate symmetric rechargeable sodium-ion batteries. Nature communications 6:6954

9. Liu Y, Qiao Y, Zhang W et al (2015) Sodium storage in Na-rich NaxFeFe (CN) 6 nanocubes. Nano Energy 12:386–393

10. Song W, Wu Z, Chen J et al (2014) High-voltage NASICON sodium ion batteries: merits of fluorine insertion. Electrochim Acta 146:142–150

11. Rajagopalan R, Tang Y, Ji X et al (2020) Advancements and challenges in potassium ion batteries: a comprehensive review. Adv Func Mater 30:1909486

12. Cao Y, Liu Y, Chen T et al (2018) Sol-gel synthesis of porous Na3Fe2(PO4)3 with enhanced sodium-ion storage capability. Ionics 25:1083–1090

13. Cao Y, Yang C, Liu Y et al (2020) A new polyanion Na3Fe(PO4)P2O7 cathode with high electrochemical performance for sodium-ion batteries. ACS Energy Lett 5:3788–3796

14. Li G, Cao Y, Chen J et al (2024) Entropy-enhanced multi-doping strategy to promote the electrochemical performance of Na4Fe3(PO4)2P2O7. Small Methods 2301745

15. Liu Z, Cao Y, Zhang H et al (2024) Towards high-performance sodium-ion batteries via the phase regulation strategy. ACS Sustainable Chemistry & Engineering 12:1132–1141

16. Zhang H, Cao Y, Liu Z et al (2024) Structurally modulated Na4–xFe3–xVx(PO4)2P2O7 by vanadium doping for long-life sodium-ion batteries. ACS Sustain Chem Eng 12:5310–5318

17. Song W, Ji X, Chen J et al (2015) Mechanistic investigation of ion migration in Na 3 V 2 (PO 4) 2 F 3 hybrid-ion batteries. Phys Chem Chem Phys 17:159–165

18. Bianchini M, Xiao P, Wang Y et al (2017) Additional sodium insertion into polyanionic cathodes for higher-energy Na-ion batteries. Adv Energy Mater 7:1700514

19. Yi G-D, Fan C-L, Hu Z et al (2021) Construction of high performance N-doped Na3V2 (PO4) 2F3/C cathode assisting by plasma enhanced chemical vapor deposition for sodium-ion batteries. Electrochim Acta 383:138370

20. Olchowka J, Nguyen LH, Broux T et al (2019) Aluminum substitution for vanadium in the Na 3 V 2 (PO 4) 2 F 3 and Na 3 V 2 (PO 4) 2 FO 2 type materials. Chem Commun 55:11719–11722

21. Criado A, Lavela P, Pérez-Vicente C et al (2020) Effect of chromium doping on Na3V2 (PO4) 2F3@ C as promising positive electrode for sodium-ion batteries. J Electroanal Chem 856:113694

22. Liu Q, Meng X, Wei Z et al (2016) Core/double-shell structured Na3V2 (PO4) 2F3@ C nanocomposite as the high power and long lifespan cathode for sodium-ion batteries. ACS Appl Mater Interfaces 8:31709–31715

23. Zhu W, Liang K, Ren Y (2021) Modification of the morphology of Na3V2 (PO4) 2F3 as cathode material for sodium-ion batteries by polyvinylpyrrolidone. Ceram Int 47:17192–17201

24. Jiang T, Chen G, Li A et al (2009) Sol–gel preparation and electrochemical properties of Na3V2 (PO4) 2F3/C composite cathode material for lithium ion batteries. J Alloy Compd 478:604–607

25. Deng L, Sun G, Goh K et al (2019) Facile one-step carbothermal reduction synthesis of Na3V2 (PO4) 2F3/C serving as cathode for sodium ion batteries. Electrochim Acta 298:459–467

26. Zhang Y, Wang T, Tang Y et al (2021) In situ redox reaction induced firmly anchoring of Na3V2 (PO4) 2F3 on reduced graphene oxide & carbon nanosheets as cathodes for high stable sodium-ion batteries. J Power Sources 516:230515

27. Li Y, Liang X, Zhong G et al (2020) Fiber-shape Na3V2 (PO4) 2F3@ N-doped carbon as a cathode material with enhanced

cycling stability for Na-ion batteries. ACS Appl Mater Interfaces 12:25920–25929

28. Mukherjee A, Sharabani T, Perelshtein I et al (2020) Three-sodium ion activity of a hollow spherical Na3V2 (PO4) 2F3 cathode: demonstrating high capacity and stability. Batteries Supercaps 3:52–55

29. Sadezky A, Muckenhuber H, Grothe H et al (2005) Raman microspectroscopy of soot and related carbonaceous materials: spectral analysis and structural information. Carbon 43:1731–1742

30. Wang C, Shen W, Liu H (2014) Nitrogen-doped carbon coated Li 3 V 2 (PO 4) 3 derived from a facile in situ fabrication strategy with ultrahigh-rate stable performance for lithium-ion storage. New J Chem 38:430–436

31. Ito Y, Cong W, Fujita T et al (2015) High catalytic activity of nitrogen and sulfur co-doped nanoporous graphene in the hydrogen evolution reaction. Angew Chem Int Ed 54:2131–2136

32. Deng L, Yu F-D, Xia Y et al (2021) Stabilizing fluorine to achieve high-voltage and ultra-stable Na3V2 (PO4) 2F3 cathode for sodium ion batteries. Nano Energy 82:105659